Effect of a straight coast on the hydrodynamics and performance of the Oscillating Wave Surge Converter

Dripta Sarkar[a,*], Emiliano Renzi[a], Frederic Dias[a,b]

[a] *UCD School of Mathematical Sciences, University College Dublin, Belfield, Dublin-4, Ireland.*
[b] *Centre de Mathematiques et de Leurs Applications (CMLA), Ecole Normale Superieure de Cachan, 94235 Cachan, France*

Abstract

This paper describes the behaviour of a flap-type oscillating wave energy converter near a straight coast. The mathematical formulation is based on a linear potential flow model. Application of Green's theorem to a semi-infinite fluid domain yields a hypersingular integral equation for the velocity potential which is solved using a series expansion of Chebyshev polynomials. Extremes in the hydrodynamic characteristics of the system are shown to occur at certain wave periods when the device is located at specific distances from the coast. This dynamics can have either detrimental or favourable effects on the performance of the converter, depending on the system parameters. Surprisingly, when the device is located very close to the coast, the qualitative behaviour of the system resembles that of a single device in the open ocean. In addition, the analysis shows that under such circumstances, the device consistently achieves much higher levels of efficiency than it would achieve in an open ocean.

Keywords:

1. Introduction

The Oscillating Wave Surge Converter (OWSC) is a buoyant flap-type wave energy converter. With the OWSC emerging as one of the frontrunners in the pursuit of harnessing energy from the ocean (Whittaker and Folley,

*Corresponding author
Email address: dripta.sarkar.1@ucdconnect.ie (Dripta Sarkar)

2012), there is a growing interest in understanding its behaviour in the context of various physical environments. Recently, Renzi and Dias developed the first theoretical models of the OWSC in a channel (Renzi and Dias, 2012), of an infinite array of OWSCs (Renzi and Dias, 2013b) and of a single OWSC in the open ocean (Renzi and Dias, 2013a). However, the effect of a straight coast on the performance of the OWSC has not been investigated yet. Such an analysis is extremely relevant for the device under investigation, since proposed OWSC wave farms are to be located in shallow waters along the rocky coasts of western Ireland and Scotland (see for example Aquamarine Power Limited, 2012). So far, few studies have tried to investigate the behaviour of wave energy converters (WECs) near a coast (Evans, 1988; Martins-Rivas and Mei, 2009; Lovas et al., 2010). In particular, (Evans, 1988) studied the variation of maximum efficiency of a point absorber in front of a vertical coastline. He observed the occurrence of peaks in the efficiency of the device when the latter is placed at specific distances from the coast. However, (Evans, 1988) did not provide an explanation of such behaviour. At the state of the art, the following research questions are still unanswered: How is the hydrodynamics of a flap-type WEC in front of a straight coast altered in relation to that in the open ocean? And if there are any significant differences in the hydrodynamic behaviour, then how does that impact the performance of the device? (Evans and Porter, 1996) had shown that for a thin vertical rolling plate in water of finite depth and in front of a rigid vertical wall, there is extreme resonance in the hydrodynamic coefficients for a frequency corresponding to the first sloshing mode between two infinitely long vertical barriers. However, it is uncertain as to how such resonance would affect the performance of similar systems used for energy capture. (Srokosz and Evans, 1979) have shown that for a system of two independent vertical rolling power absorbers in infinite water depth, nearly 100% power capture is in fact possible. However, complete absorption of energy could not be achieved due to the finite length of the plates, which results in leakage of energy beneath them. But both the studies of (Evans and Porter, 1996) and (Srokosz and Evans, 1979) are two-dimensional and are therefore insufficient to describe the behaviour of the systems in a three-dimensional wave field.

In this paper, following the procedure of (Renzi and Dias, 2012), a three dimensional mathematical model is developed based on the assumption of the fluid being inviscid and incompressible and the flow irrotational. The approach has been extended and used to analyse the behaviour of the OWSC in the open ocean (Renzi and Dias, 2013a), inline array (Renzi et al., 2014),

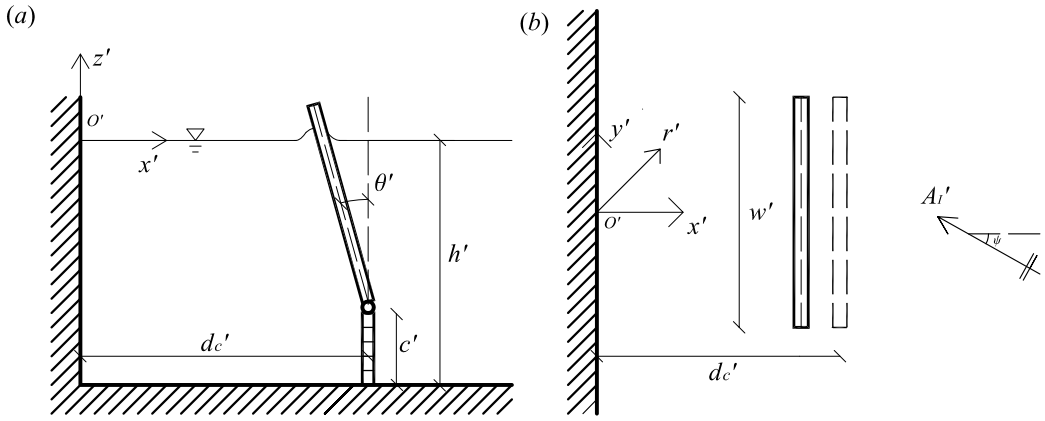

Figure 1: Geometry of the model (a) cross-section (b) top view

wavefarm (Sarkar et al., 2014b), and its interaction with a Heaving Wave Energy Converter (Sarkar et al., 2014a). The semi-analytical model is based on the thin-rigid plate hypothesis and has been validated against results from experimental and numerical works (see Renzi and Dias, 2012; Renzi et al., 2014). The good agreement is primarily because the thickness of the OWSC is much small compared to its width - the characteristic dimension of the device.

The analysis in this work is performed using Green's integral theorem and Green's function for a semi-infinite domain. The linearity of the problem facilitates its decomposition into two separate - radiation and scattering - components. The variations of the excitation torque and of the radiation coefficients are discussed in §3. The effect of the hydrodynamic behaviour on the device performance is then investigated. It is shown that the presence of the vertical barrier on the leeward side of the OWSC has in general an 'oxymoronic' kind of effect on the device performance. However, a significant enhancement in the performance of the device across its entire operating range, is possible, when it is located very close to the coast.

2. Mathematical Model

2.1. Governing Equations

Consider an OWSC of width w' located in an ocean of constant water depth h' and at a distance d_c' away from the coastline, represented as a

fully reflecting vertical barrier as shown in figure 1. Primes denote physical dimensional variables. The origin of the co-ordinate system is located on the mean free surface at the intersection of the straight coast and the vertical plane passing through the centre of the flap and perpendicular to the coast. The x' axis is directed outwards from the vertical barrier, the y' axis is directed along the coast and z' points upwards. The flap is hinged to a bottom foundation and oscillates about the horizontal axis located at a distance $h'-c'$ from the mean free surface. Monochromatic waves of amplitude A'_I and period T' incident from the right, making an angle ψ with the x'-axis cause the flap to oscillate, thereby extracting energy from a generator linked to it. The amplitude of the waves is considered to be small such that $A'_I/w' \ll 1$. As a consequence, the governing equations of motion can be linearised by taking only the first-order terms of the perturbation series expansion in A'_I/w' (see Renzi and Dias, 2012) . The velocity potential Φ' satisfies the Laplace equation

$$\nabla'^2\Phi' = 0, \tag{1}$$

in the fluid domain, where $\nabla' f' = (f'_{,x'}, f'_{,y'}, f'_{,z'})$ is the nabla operator; subscript with commas denote differentiation with respect to relevant variables. The linearised kinematic-dynamic boundary condition on the free surface gives

$$\Phi'_{,t't'} + g\Phi'_{,z'} = 0, \qquad z' = 0, \tag{2}$$

where g is the acceleration due to gravity. The no-flux condition at the sea bed gives

$$\Phi'_{,z'} = 0, \qquad z' = -h', \tag{3}$$

while the absence of normal flow through the vertical barrier results in

$$\Phi'_{,x'} = 0, \qquad x' = 0. \tag{4}$$

Finally the kinematic condition on the lateral surfaces of the flap yields

$$\Phi'_{,x'} = -\theta'_{,t'}(z'+h'-c')H(z'+h'-c'), \qquad x' = d'_c \pm \varepsilon', \varepsilon' \to 0, \qquad |y'| < \frac{w'}{2}, \tag{5}$$

where thin plate approximation has been used (see Linton and McIver, 2001; Renzi and Dias, 2012). In (5), $\theta'(t')$ is the unknown amplitude of oscillation of the flap, positive if anticlockwise (see again figure 1), while H is the Heaviside step function.

2.2. Solution

Let us introduce the non-dimensional system of variables as follows

$$(x, y, z, d_c, r) = (x', y', z', d'_c, r')/w', t = \sqrt{\frac{g}{w'}}t', \Phi = \frac{\Phi'}{\sqrt{gw'}A'_I}, \theta = (w'/A'_I)\theta', \tag{6}$$

where $r' = \sqrt{x'^2 + y'^2}$. Assuming the oscillations of the flap to be simple harmonic in nature, the time dependence of the variables can be separated out as

$$\theta = Re\{\Theta e^{-i\omega t}\}, \qquad \Phi = Re\{(\phi^R + \phi^S)e^{-i\omega t}\}, \tag{7}$$

where $\omega = \omega'\sqrt{w'/g}$ and Θ are respectively, the angular frequency and amplitude of oscillation of the flap, while $\phi^R(x, y, z)$ and $\phi^S(x, y, z)$ are the complex spatial radiation and scattering potential, respectively. The scattering potential can in turn be resolved into

$$\phi^S = \phi^I + \phi^F + \phi^D \tag{8}$$

where

$$\phi^I = -\frac{iA_I}{\omega}\frac{\cosh k(z+h)}{\cosh kh}e^{-ikx\cos\psi + iky\sin\psi} \tag{9}$$

and

$$\phi^F = -\frac{iA_I}{\omega}\frac{\cosh k(z+h)}{\cosh kh}e^{ikx\cos\psi + iky\sin\psi}. \tag{10}$$

In (8), ϕ^I is the incident wave potential, ϕ^F the potential of the reflected wave from the coast and ϕ^D the diffracted wave potential, which is unknown. On substitution of the factorisation (7) and (8) in the governing equations (1)–(5), we obtain a boundary-value problem in terms of the spatial radiation and scattering potentials. The latter satisfy the Laplace equation

$$\nabla^2\phi^{(R,D)} = 0, \tag{11}$$

where the notation $\phi^{(R,D)}$ denotes either potential, the linearised free-surface boundary condition

$$-\omega^2\phi^{(R,D)} + \phi^{(R,D)}_{,z} = 0, \qquad z = 0, \tag{12}$$

the no-flux boundary conditions at the sea bed and at the straight coast

$$\phi^{(R,D)}_{,z} = 0, \qquad z = -h, \tag{13}$$

$$\phi^{(R,D)}_{,x} = 0, \qquad x = 0, \tag{14}$$

respectively, and the kinematic conditions

$$\left\{ \begin{array}{c} \phi^R_{,x} \\ \phi^D_{,x} \end{array} \right\} = \left\{ \begin{array}{r} V(z+h-c)H(z+h-c) \\ -\phi^I_{,x} - \phi^F_{,x} \end{array} \right\} \qquad x = d_c \pm \varepsilon, \varepsilon \to 0, \quad |y| < \frac{1}{2}, \tag{15}$$

on the lateral surfaces of the flap. Finally, both ϕ^R and ϕ^D are required to be outgoing disturbances of the wave field (Mei et al., 2005). In (15) $V = i\omega\Theta$ and the thin plate approximation has been used (see Renzi and Dias, 2012; Linton and McIver, 2001). The vertical dependence can now be isolated out of the three dimensional governing system (11)–(15) by using the separation (see Mei et al., 2005)

$$\phi^{(R,D)}(x,y,z) = \sum_{n=0}^{\infty} \varphi^{(R,D)}_n(x,y) Z_n(z), \tag{16}$$

where

$$Z_n(z) = \frac{\sqrt{2}\cosh\kappa_n(z+h)}{(h+\omega^{-2}\sinh^2\kappa_n h)^{1/2}}, \tag{17}$$

are the normalised vertical eigenmodes satisfying the orthogonality relation

$$\int_{-h}^{0} Z_n(z) Z_m(z) dz = \delta_{nm}, \tag{18}$$

δ_{nm} being the Kronecker delta. In (17), $\kappa_0 = k$ and $\kappa_n = ik_n$ are the solutions of the dispersion relation

$$\omega^2 = k\tanh kh, \quad \omega^2 = -k_n \tan k_n h, n = 1, 2, ... \tag{19}$$

respectively.

Using the decomposition (16) and the orthogonality relation (18) yields a two-dimensional governing system for $\varphi^{(R,D)}_n$, where the Laplace equation (11) becomes the Helmholtz equation

$$(\nabla^2 + \kappa_n^2)\varphi^{(R,D)}_n = 0, \tag{20}$$

the no-flux condition at the straight coast (14) transforms into

$$\varphi^{(R,D)}_{n,x} = 0, \quad x = 0, \tag{21}$$

and the kinematic condition on the flap (15) becomes

$$\left\{ \begin{array}{c} \varphi^R_{n,x} \\ \varphi^D_{n,x} \end{array} \right\} = \left\{ \begin{array}{c} V f_n \\ A_I d_n \end{array} \right\} \qquad x = d_c \pm \varepsilon, \varepsilon \to 0, \quad |y| < \frac{1}{2}. \tag{22}$$

In the latter

$$f_n = \frac{\sqrt{2}[\kappa_n(h-c)\sinh(\kappa_n h) + \cosh(\kappa_n c) - \cosh(\kappa_n h))]}{\kappa_n^2(h + \omega^{-2}\sinh^2(\kappa_n h))^{1/2}} \tag{23}$$

and

$$d_n = -\frac{\sqrt{2}ik\cos\psi\sin(k\cos\psi d_c)}{\omega\cosh kh}(h + \omega^{-2}\sinh^2 kh)^{1/2}\delta_{0,n} \tag{24}$$

are constants depending on the geometry of the system. Finally the $\varphi_n^{(R,D)}$ must be outgoing disturbances for $r \to \infty$. Following the method of (Renzi and Dias, 2012), the boundary value problem (20) – (22) is solved using Green's integral equation formulation and appropriate Green's function for the semi-infinite fluid domain. The procedure, described in Appendix A, allows one to obtain a solution for the spatial velocity potentials $\phi^{(R,D)}$ (16) as a fast converging semi-analytical form. As a result, the radiation potential is expressed as

$$\begin{aligned} \phi^R(x,y,z) = -\frac{i}{8}V\sum_{n=0}^{+\infty}\kappa_n Z_n(z)\sum_{p=0}^{P}\alpha_{pn}\int_{-1}^{1}(1-u^2)^{1/2}U_p(u)\times \\ \left\{\frac{H_1^{(1)}\left(\kappa_n\sqrt{(x-d_c)^2+(y-\frac{u}{2})^2}\right)}{\sqrt{(x-d_c)^2+(y-\frac{u}{2})^2}}(x-d_c)\right. \\ \left.-\frac{H_1^{(1)}\left(\kappa_n\sqrt{(x+d_c)^2+(y-\frac{u}{2})^2}\right)}{\sqrt{(x+d_c)^2+(y-\frac{u}{2})^2}}(x+d_c)\right\}du, \end{aligned} \tag{25}$$

where $H_1^{(1)}$ is the Hankel function of the first kind and first order, U_p is the Chebyshev polynomial of the second kind and order p, $p = 0, 1, .., P \in \mathbb{N}$ and the α_{pn} are the complex solutions of a system of equations, which is

solved numerically using a collocation scheme (see Appendix A for details). Similarly, the diffraction potential is given by

$$\phi^D(x,y,z) = -\frac{i}{8}A_I k Z_0(z)\sum_{p=0}^{P}\beta_{p0}\int_{-1}^{1}(1-u^2)^{1/2}U_p(u)\times \\ \left\{\frac{H_1^{(1)}\left(k\sqrt{(x-d_c)^2+(y-\frac{u}{2})^2}\right)}{\sqrt{(x-d_c)^2+(y-\frac{u}{2})^2}}(x-d_c)\right. \\ \left.-\frac{H_1^{(1)}\left(k\sqrt{(x+d_c)^2+(y-\frac{u}{2})^2}\right)}{\sqrt{(x+d_c)^2+(y-\frac{u}{2})^2}}(x+d_c)\right\}du, \qquad (26)$$

where the β_{p0} are the complex solutions of a system of equations, again solved numerically. Note that in ϕ^D (26) only the 0th order vertical mode is present, the flap being a walled structure in the scattering problem (i.e $\varphi_n^D = 0$ for $n > 0$). Using the above expressions (25) and (26), the equation of motion of the flap can be now solved.

2.3. Hydrodynamic Parameters

The non-dimensional equation of motion of the flap in the frequency domain is that of a damped harmonic oscillator (see Mei et al., 2005; Renzi and Dias, 2013a) :

$$[-\omega^2 I + C - i\omega\nu_{pto}]\Theta = \mathbf{F}. \qquad (27)$$

In the latter, $I = I'/(\rho w'^5)$ is the second moment of inertia of the flap, $C = C'/(\rho g w'^4)$ the coefficient of the net restoring flap buoyancy torque, $\nu_{pto} = \nu'_{pto}/(\rho w'^5\sqrt{g/w'})$ the power take-off (PTO) damping coefficient and

$$\mathbf{F} = i\omega\int_{-h+c}^{0}\int_{-1/2}^{1/2}\Delta\phi(z+h-c)dydz \qquad (28)$$

is the complex hydrodynamic torque, where

$$\Delta\phi = \phi(d_c-\varepsilon,y,z) - \phi(d_c+\varepsilon,y,z) \\ = [\phi^D(d_c-\varepsilon,y,z)+\phi^R(d_c-\varepsilon,y,z)] - [\phi^D(d_c+\varepsilon,y,z)+\phi^R(d_c+\varepsilon,y,z)], \qquad (29)$$

with $\varepsilon \to 0$, is the potential difference across the two sides of the flap. Using (16), (A.5) and (A.11) and decomposing the complex hydrodynamic torque due to the radiation potential into real and imaginary components, (27) finally becomes

$$[-\omega^2(I+\mu) + C - i\omega(\nu + \nu_{pto})]\Theta = F, \tag{30}$$

where

$$\mu = \frac{\pi}{4} Re\left\{ \sum_{n=0}^{\infty} f_n \alpha_{0n} \right\} \tag{31}$$

is the added inertia due to the torque,

$$\nu = \frac{\pi\omega}{4} Im\left\{ \sum_{n=0}^{\infty} f_n \alpha_{0n} \right\} \tag{32}$$

is the radiation damping and

$$F = -\frac{\pi\omega}{4} i A_I \beta_{00} f_0 \tag{33}$$

is the excitation torque. According to the theory of damped oscillating systems (see Falnes, 2002), the average extracted power by the generator over a wave period is

$$P = \frac{1}{2} \frac{\omega^2 \nu_{pto} |F|^2}{[C - (I+\mu)\omega^2]^2 + (\nu + \nu_{pto})^2 \omega^2}. \tag{34}$$

To obtain the optimal PTO damping for maximum power capture away from body resonance (see Renzi and Dias, 2012, 2013a,b), we need $\partial P / \partial \nu_{pto} = 0$, which gives

$$\nu_{pto} = \sqrt{\frac{[C - (I+\mu)\omega^2]^2}{\omega^2} + \nu^2}, \tag{35}$$

and the optimum generated power is

$$P_{opt} = \frac{|F|^2}{4(\nu_{pto} + \nu)}. \tag{36}$$

In order to quantify the efficiency of the device, the capture factor is used which is defined as the ratio of the power extracted by the device per unit flap width to the incident wave power per unit crest width, i.e.

$$C_F = \frac{P_{opt}}{\frac{1}{2} C_g A_I^2}, \tag{37}$$

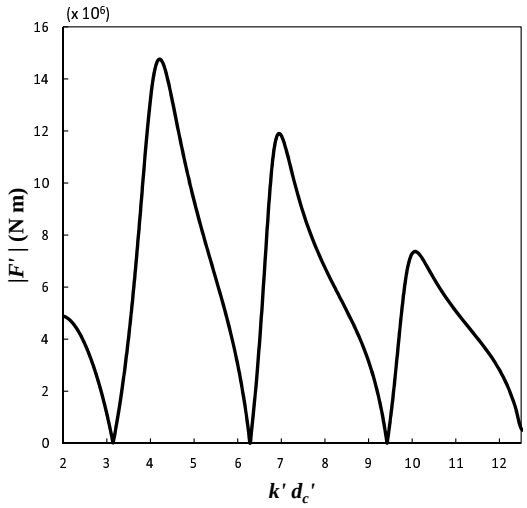

Figure 2: Behaviour of excitation torque $|F'| = |F|\rho g A_I' w'^3$ (see 33). Parameters are $w' = 26$m, $d_c' = 50$m, $h' = 13$m, $c' = 4$m, $\psi = 0^\circ$ and $A_I' = 0.3$m.

where

$$C_g = \frac{\omega}{2k}\left(1 + \frac{2kh}{\sinh 2kh}\right) \tag{38}$$

is the group velocity of the incident waves. In the next section, the behaviour of the hydrodynamic parameters of the system is discussed. Parametric analysis is then undertaken which shows the sensitivity of the system with respect to the distance d_c' between the flap and the coast.

3. Discussion

In this section, the behaviour of the hydrodynamic parameters derived in §2.3 is discussed. Numerical computations are performed with a flap of width $w' = 26$m, in water of depth $h' = 13$m and with the distance $c' = 4$m. The values of the physical variables closely resemble those of the newer version of the flap-type wave energy conversion device Oyster800 developed by Aquamarine Power Ltd. (www.aquamarinepower.com). Computations performed in this study are shown only for normally incident waves (i.e. $\psi = 0^\circ$) since, in shallow waters the incoming wave fronts are predominantly orthogonal to the shoreline, which is also known to let the OWSC generate

maximum power (see Whittaker and Folley, 2012). In fact normal wave incidence is common in practice with this device (see Renzi and Dias, 2012, 2013a,b).

3.1. Excitation Torque

The variation of the excitation torque versus the non-dimensional parameter $k'd'_c = kd_c$ is shown in figure 2 for $d'_c = 50$m. Zeros in the excitation torque occur for $k'd'_c = m\pi$, $m = 1, 2, ..$, while maxima are slightly below the intermediate locations between two neighbouring zeros, i.e. $k'd'_c \simeq (m + 1/2)\pi$, $m = 1, 2, ...$ Such behaviour can be explained with the following argument. Let us consider a semi-infinite fluid domain in the absence of the flap. In steady state, the interaction of the incident and reflected waves from the straight coast leads to the formation of a two-dimensional standing wave field, as illustrated in figure 3. The locations $k'd'_c = m\pi$ correspond to the antinodes of the standing wave field, where the movements of the water particles are in the vertical direction (see Dean and Dalrymple, 1991). Now consider wave diffraction by a flap held fixed in its upright position, located at one of the antinodes of the standing wave field represented in figure 3. In this configuration, the no-flux boundary condition at the flap lateral surfaces is satisfied automatically and, being of negligible thickness, the flap apparently does not introduce any discontinuity in the wave field. In other words, the flap pretends as if it is invisible to the wave field. As a consequence, there is no diffracted wave, which manifests as zero excitation torque on the flap for $k'd'_c = m\pi$, as obtained in the simulations of figure 2. However, for locations of the flap different from those mentioned above, a three-dimensional (3D) diffracted wave field is produced, as a deviation from the original 2D configuration.

Such deviation is naturally stronger near the locations $kd_c = (m+1/2)\pi$, $m = 0, 1, 2, ...$, corresponding to the nodes of the standing waves where the trajectories are horizontal, and results in the resonant peaks of figure 2. Those are slightly below $k'd'_c = (m + 1/2)\pi$, due to the radial dispersion of the 3D scattered wave field, which represents a source of damping for the system and lowers its resonant periods with respect to the 2D scenario.

3.2. Radiation parameters

The behaviours of the added inertia torque and the radiation damping are shown in figure 4 for the same configuration as above. Spikes in added inertia and radiation damping coefficients are observed, each below $k'd'_c = (m +$

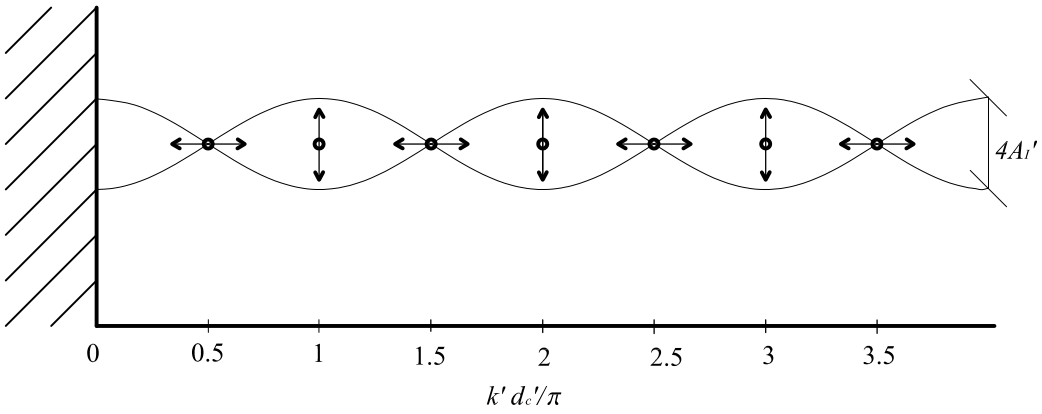

Figure 3: Particle trajectory in a standing wave field.

$1/2)\pi, m = 1, 2, \ldots$. This behaviour, although different, has some similarity with that of the antisymmetric modes of motion of a thin vertical plate lying on the centreline of a straight channel of width $2d_c'$ and aligned with the channel walls (see Linton and Evans, 1993). For such a system, (Linton and Evans, 1993) found that the radiation coefficients for sway motion exhibit sharp spiky but non-singular behaviour at frequencies a little below $k'd_c' = (m + 1/2)\pi$. Each of the latter corresponds to a simple pole in the lower half of the complex frequency plane. Linton and Evans (1993) also showed that the complex force coefficient $F_c = \nu + i\mu$ traces a circle as ω moves on the real axis close to the pole and that the total extent of the spikes in radiation coefficients correspond to the diameter of the circle.

The system analysed here can be thought of to be the vertical flap of Linton and Evans (1993) with the straight coast as one of the channel walls while the other wall is absent. Compared with the sharp spikes of (Linton and Evans, 1993), the variation in added inertia and radiation damping of figure 4 exhibits blunt peaks with wider bandwidth, suggesting an imperfect form of resonance. Note that the peaks in radiation damping correspond to locations $k'd_c'$ which are halfway between two neighbouring extremes in added inertia. This is also similar to the behaviour of the radiation coefficients in Linton and Evans (1993). However there are some notable differences between the two systems. The variation of the complex force coefficient as ω moves on the real axis is plotted in figure 5 for the system of figure 4. First, note that the complex force coefficient shown in figure 5, follows approximate ellipses rather

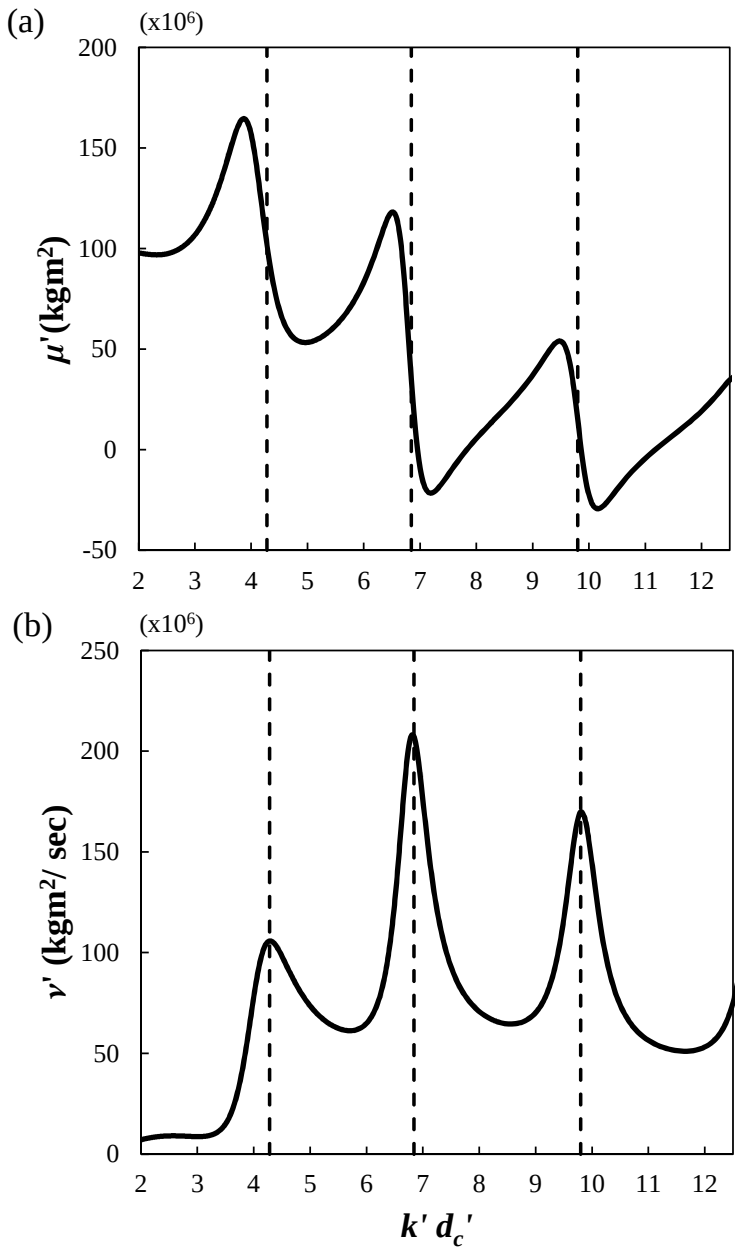

Figure 4: Behaviour of (a) added inertia ($\mu = \mu'/\rho w'^5$, see 31) (b) radiation damping ($\nu = \nu'/(\rho w'^4\sqrt{gw'})$, see 32) for $w' = 26$m, $d'_c = 50$m, $h' = 13$m, $c' = 4$m, $\psi = 0°$ and $A'_I = 0.3$m . The vertical lines indicate the location of the peaks in radiation damping: $k'd'_c = 4.28, 6.84$ and 9.8.

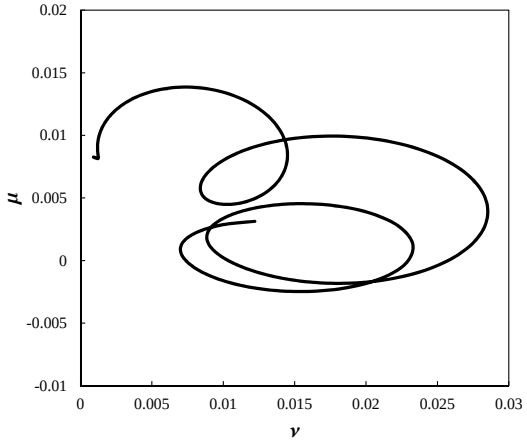

Figure 5: Path of the complex force coefficient $F_c = \nu + i\mu$ as ω moves on the real axis, showing the variation of added inertia coefficient μ versus radiation damping coefficient ν for $d'_c = 50$m. The parameters of the system are those of figure 4.

than circles (as in Linton and Evans, 1993), due to the unequal extent of the spikes in added inertia and radiation damping coefficients. Second, the traces of the ellipses do not go through the origin. This is because the magnitude of the radiation coefficients ν and μ away from the resonant locations is not insignificant compared to the peaks, as opposed to the channel problem. Lastly, unlike in Linton and Evans (1993), the trace of the complex force coefficient never completes any particular orbit in the (ν, μ) plane (see again figure 5). This is due to a likely shift of the poles further away from the real axis, because of the larger dissipation of energy by radiation in the straight coast problem than in the channel. Since each pole is further away from the real axis, the neighbouring poles now influence the variation of F_c. As a consequence, the complex force moves on a near elliptical orbit as ω moves on the real axis close to a particular pole. However, as ω moves further away from that particular pole, the influence of the neighbouring pole becomes increasingly dominant and therefore F_c cannot complete a particular orbit and moves to another orbit.

3.3. Energy Capture

Figure 6(a) shows the behaviour of the amplitude of rotation $|\Theta'|$ versus the parameter $k'd'_c$. Unlike in the open ocean, where the amplitude of rotation of the flap increases monotonically versus the incident wave period (Renzi

and Dias, 2013a), in the present configuration the effect of the vertical barrier results in alternate maxima and minima in the amplitude curve (see figure 6a). The minima occur at $k'd'_c = m\pi$ and correspond to the flap coming to a stand still in its vertically upright position when the exciting torque is zero (see figure 2). The maxima, on the other hand, are less predictable and lie somewhere in between the locations of the peak excitation torque (see figure 2) and the troughs of the radiation coefficients (figure 4). Figure 6 (b) shows the plot of the capture factor C_F (37) versus $k'd'_c$ for $d'_c = 50$m. Again, the positions of the minima are absolutely determined, corresponding to the flap being motionless in standing waves. On the other hand, the positions of the maxima are less predictable, due to the combined influence of the various parameters in (37) and (34). Note that figure 6 (b) reminds the behaviour of the capture factor curve for a two-dimensional system of two independently oscillating vertical flaps studied by Srokosz and Evans (1979). The latter showed that under resonant conditions, such a system can achieve maximum efficiency (i.e. capture factor of 1). The analysis was however two-dimensional. In 3D, appropriate phases of the reflected wave field can create a larger potential difference across the two sides of the flap than in 2D, producing larger excitation torques. This coupled with the fact that the structure of the 3D wave field around the oscillating flap assists in capturing larger power (see Renzi and Dias, 2012), raises the maximum capture factor for the 3D problem under consideration.

3.4. Parametric Analysis

The variation of power capture shown in figure 6(b) suggests that even a slight movement away from the peak periods would drastically reduce the performance of the device and could even lead to no power capture at all. Therefore, from a designer's perspective, the challenge is to avert such detrimental effects on the device performance by identifying a layout in which the zeros of power capture can be avoided for a given frequency range of the incident waves. As already shown in figure 6(b), the zeros of C_F occur each time the parameter $k'd'_c/\pi$ passes through a positive integer value. This would suggest that to avoid the zeros, it must be $\max(k')d'_c/\pi < 1$, which would mean $d'_c < \min\lambda'/2$, i.e. the distance d'_c should be within half a wavelength of the smallest wave considered. This would then circumvent the possibility of the flap being located at an anti-node of the standing wave field (see again figure 3).

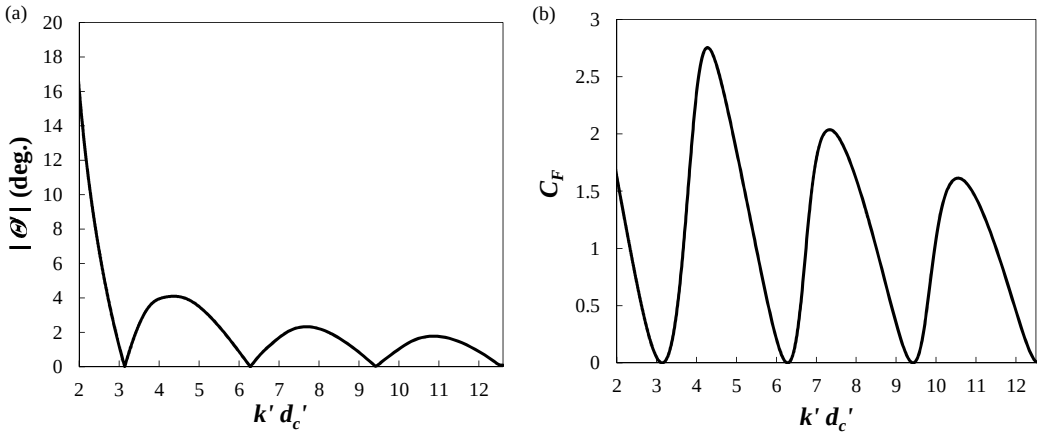

Figure 6: Behaviour of (a) amplitude of rotation and (b) capture factor with $k'd'_c$ in physical variables for $d'_c = 50$m. The values of the other physical variables are as mentioned in §3.

As an example, the behaviour of the excitation torque versus $k'd'_c$ and time period T' is plotted in figure 7 and figure 8 shows the variation of the capture factor C_F with time period T'. In both figures, $d'_c = 12$m and $k'd'_c < \pi$. In this configuration, not only the zeros of the excitation torque are avoided (see figure 7) but also a significant enhancement in the average capture factor over that in an open ocean is observed (see figure 8). This suggests that the presence of the coast can have a strong beneficial influence on the device performance if the distance d'_c is appropriately chosen. The enhancement is primarily due to the magnification in excitation torque which interestingly occurs at $k'd'_c$ values much less than $\pi/2$.
Although the capture factor depends on multiple parameters - excitation torque, radiation damping, added inertia, PTO damping; the dynamics of the OWSC is strongly governed by the diffraction phenomenon, and hence the performance is strongly correlated with the excitation torque. In fact the power captured (and therefore the capture factor) is proportional to the square of the excitation torque (see equation 34). The peak of the excitation torque in the straight coast problem is more than twice that in the open ocean, which consequently makes the peak in the capture factor nearly four times than that in the later case (see figures 7 and 8).

3.5. OWSCs, point absorbers, future research directions and other aspects

As mentioned earlier, Evans (1988) studied the performance of a point absorber near a straight coast. In the case of normal incidence, a similar irregular behaviour in the performance of the point absorbers was observed, with periodic occurrence of maxima and minima in the variation of maximum efficiency with $k'd'_c$. However, for the point absorber the capture factor is zero when $k'd'_c \simeq (m+1/2)\pi$, while it is maximum at $k'd'_c = m\pi$. This behaviour is in contrast and exactly opposite to that of the OWSC (see again figure 6 b) and can be explained in the following manner. The locations $k'd'_c = m\pi$ correspond to the antinodes of the standing wave field where the movement of the water particles is completely vertical. On the other hand, $k'd'_c = (n+1/2)\pi$ corresponds to the nodes where the movement is horizontal. The heaving point absorber utilizes the vertical movement of the water particles to capture power. Therefore it comes to a complete standstill at the nodes because of no excitation force, but captures maximum power when located at the antinodes. This simplified explanation is possible because of the small dimension of the point absorbers which produce an insignificant diffracted wave field. The OWSC exploits the amplified surge motion of the water particles in shallow water and therefore behaves conversely to the point absorber. This would then suggest that using a proper combination of OWSCs and point absorbers near a straight coast could be beneficial for enhancing the efficiency of a combined wave farm. Such investigation is envisaged as an intriguing future research direction. Also, application of linear theory restricts the analysis performed in this study to a flat bottom. Another interesting topic for future research would be to investigate the behaviour of the device on a sloped bottom using a numerical approach.

The concept of two OWSCs (Oysters) back to back has already been analysed in (Sarkar et al., 2014b). It has been shown that the front OWSC can have a significant gain or loss in the power captured depending on the distance between the two devices and the incident wave period. But the OWSC at the back always has a negative interaction effect (destructive influence) leading to a significant loss in the power captured.

The recent work of Sammarco et al (2013) (Sammarco et al., 2013) deals with the determination of natural modes of resonance of multiple rows of gates. Similar analysis for the OWSCs has been performed in Renzi and Dias (2014) where the out-of-phase motion of the OWSCs has been investigated. Such resonant motions of the OWSCs may occur at wave periods away from the operating range of the device.

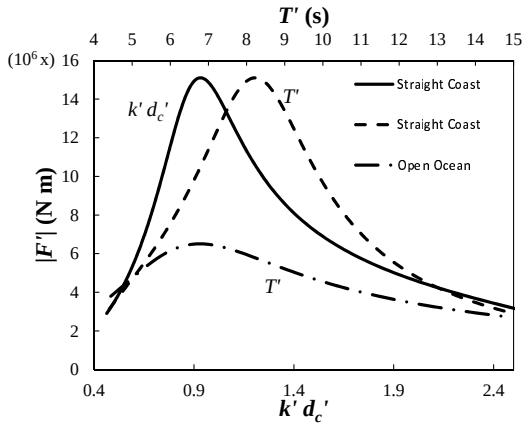

Figure 7: Behaviour of of the excitation torque $|F'|$ versus $k'd'_c$ (plotted in continuous line) and time period T' (plotted in dashed line) for $d'_c = 12$m in physical variables for the geometry of §3. The dashed-dotted line plots the variation of $|F'|$ versus T' in the open ocean case.

The analysis in this study is performed in an idealized setting. In a real sea, irregular waves, nonlinear wave interaction, bottom friction, partial reflection of waves from the coast, wave breaking, dissipation and other effects - can modify the behavior of such a system.

4. Conclusion

Using Green's function for a semi-infinite domain, a three dimensional semi-analytical method is developed to analyse the behaviour of the OWSC in front of a straight vertical coast. For locations corresponding to $k'd'_c = m\pi$, the incident, diffracted and reflected waves produce a two-dimensional standing wave field which brings the flap to a standstill. Hence the OWSC does not capture any power corresponding to these locations. The further the flap is from the coast, the higher is the number of standing wave modes for given range of monochromatic incident wave periods. Conversely, peaks in the radiation coefficient occur for $k'd'_c$ a little below the resonant frequencies $(m + 1/2)\pi$ of a swaying flap aligned with the walls of a straight channel (see Evans and Porter, 1996). Surprisingly, when located very close to a coast, the device reproduces the qualitative behaviour it would have in the open ocean, with only a single peak in the capture factor curve. For a given range of incident wave fields, it is found that the formation of the standing waves

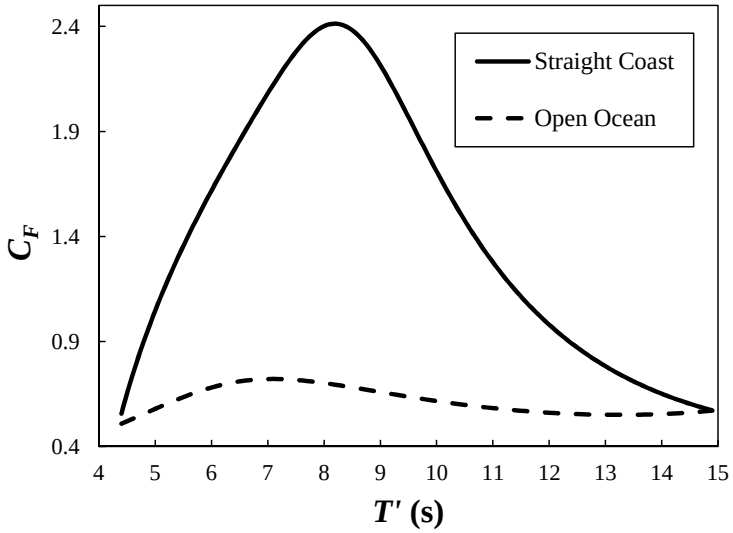

Figure 8: Comparison of the capture factors for $d'_c = 12$m and for the open ocean with the geometry of the physical system as mentioned in §3. Values for the open ocean are calculated with the model of (Renzi and Dias, 2013a)

is avoided when d'_c is less than half the wavelength of the incident wave field. Therefore one can wisely utilise the presence of a coast for capturing more power by effectively tuning the distance between the coast and the flap. Taking inspiration from the above phenomenon, one might in a realistic scenario reproduce the influence of the straight coast by introducing a long vertical breakwater on the leeward side of the OWSC, to enhance its performance. The analysis in this study is performed in an idealized setting. In a real sea, irregular waves, nonlinear wave interaction, bottom friction, partial reflection of waves from the straight coast, wave breaking and dissipation-can modify the behaviour of such a system.

Acknowledgements

This work was funded by Science Foundation Ireland under the research project " High-end computational modelling for wave energy systems". Fruitful discussions with the R & D team of Aquamarine Power Ltd. as well as with Prof. Alain Clément and Dr. Gregory Payne are kindly acknowledged.

Appendix A. Semi-analytical solution to radiation and diffraction potentials

The Green function for the semi infinite fluid domain $D = \{(x, y) : x > 0, -\infty < y < +\infty\}$ can be defined as

$$G_n(x, y; \xi, \eta) = -\frac{i}{4}\left[G_n^{(0)}(x, y; \xi, \eta) + G_n^{(1)}(x, y; \xi, \eta)\right] \tag{A.1}$$

where

$$G_n^{(0)}(x, y; \xi, \eta) = H_0^{(1)}\left(\kappa_n\sqrt{(x-\xi)^2 + (y-\eta)^2}\right) \tag{A.2}$$

and

$$G_n^{(1)}(x, y; \xi, \eta) = H_0^{(1)}\left(\kappa_n\sqrt{(x+\xi)^2 + (y-\eta)^2}\right), \tag{A.3}$$

$\xi > 0$, $-\infty < \eta < +\infty$. Application of the Green Integral theorem to the 2D radiation and diffraction potentials $\varphi_n^{(R,D)}$ and G_n in the semi infinite fluid domain D (see Mei, 1997) yields

$$\varphi_n^{(R,D)}(x, y) = -\frac{i}{4}\int_{-1/2}^{1/2} \Delta\varphi_n^{(R,D)}[G_{n,\xi}^{(0)} + G_{n,\xi}^{(1)}]\Big|_{\xi=d_c} d\eta, \tag{A.4}$$

which is similar in form to expression (B7) of (Renzi and Dias, 2012), but with different Green functions. Substituting (A.2) and (A.3) into (A.4), making the change of variables $u = 2\eta$, $v = 2y$, $u, v \in (-1, 1)$, defining

$$\left\{ \begin{array}{c} P_n(u) \\ Q_n(u) \end{array} \right\} = \left\{ \begin{array}{c} \Delta\varphi_n^R(\eta) \\ \Delta\varphi_n^D(\eta) \end{array} \right\}, \tag{A.5}$$

and then decomposing the integral (A.4) into a Hadamard finite part integral (see Linton and McIver, 2001) and a convergent integral gives

$$\kappa_n \text{⨍}_{-1}^{1} \left\{ \begin{array}{c} P_n(u) \\ Q_n(u) \end{array} \right\} \frac{H_1^{(1)}\left(\frac{1}{2}\kappa_n w|v-u|\right)}{|v-u|} du + \kappa_n \int_{-1}^{1} \left\{ \begin{array}{c} P_n(u) \\ Q_n(u) \end{array} \right\} L_n(u) du = 4i \left\{ \begin{array}{c} V f_n \\ A_I d_n \end{array} \right\}. \tag{A.6}$$

In the latter

$$L_n(u) = \left(\frac{2}{16d_c^2 + (v-u)^2} \right) \times \left[4d_c^2 \kappa_n H_2^{(1)} \left(\frac{\kappa_n}{2} \sqrt{16d_c^2 + (v-u)^2} \right) \right.$$
$$- \frac{8d_c^2 H_1^{(1)} \left(\frac{\kappa_n}{2} \sqrt{16d_c^2 + (v-u)^2} \right)}{\sqrt{16d_c^2 + (v-u)^2}}$$
$$\left. - \frac{(v-u)^2}{2\sqrt{16d_c^2 + (v-u)^2}} H_1^{(1)} \left(\frac{\kappa_n}{2} \sqrt{16d_c^2 + (v-u)^2} \right) \right], \quad \text{(A.7)}$$

where the property $H_1^{(1)'}(z) = -H_2^{(1)}(z) + H_1^{(1)}(z)/z$ has been also used (see Gradshteyn and Ryzhik, 2007). Now expand the Hankel function in the Hadamard integral of (A.6) as

$$H_1^{(1)} \left(\frac{1}{2} \kappa_n w |v-u| \right) = \frac{4}{i\pi} \frac{1}{\kappa_n w |v-u|} + R_n \left(\frac{1}{2} \kappa_n w |v-u| \right), \quad \text{(A.8)}$$

where

$$R_n(\alpha) = J_1(\alpha) \left[1 + \frac{2i}{\pi} \left(\ln \frac{\alpha}{2} + \gamma \right) \right] - \frac{i}{\pi} \left[\frac{\alpha}{2} + \sum_{j=2}^{+\infty} \frac{(-1)^{j+1} (\alpha/2)^{2j-1}}{j!(j-1)!} \left(\frac{1}{j} + \sum_{q=1}^{j-1} \frac{2}{q} \right) \right] \quad \text{(A.9)}$$

is the remainder, $J_1(\alpha)$ is the Bessel function of first kind and first order, and $\gamma = 0.577215....$ is the Euler constant (see Gradshteyn and Ryzhik, 2007). Then substitute (A.8) into (A.6) to obtain

$$\not\int_{-1}^{1} \left\{ \begin{array}{c} P_n(u) \\ Q_n(u) \end{array} \right\} \frac{1}{\kappa_n w |v-u|^2} du + \frac{i\pi\kappa_n w}{4} \int_{-1}^{1} \left\{ \begin{array}{c} P_n(u) \\ Q_n(u) \end{array} \right\} \times$$
$$\left[L(u) + \frac{R_n\left(\frac{1}{2}\kappa_n w |v-u|\right)}{|v-u|} \right] du = -\pi w \left\{ \begin{array}{c} V f_n \\ A_I d_n \end{array} \right\}, \quad \text{(A.10)}$$

where P_n Q_n are, respectively, the jump in radiation and diffraction potentials across the flap in the new variables. The structure of (A.10) suggests to seek a solution of the form

$$\left\{ \begin{array}{c} P_n(u) \\ Q_n(u) \end{array} \right\} = \left\{ \begin{array}{c} V \\ A_I \end{array} \right\} (1-u^2)^{1/2} \sum_{p=0}^{+\infty} \left\{ \begin{array}{c} \alpha_{pn} \\ \beta_{pn} \end{array} \right\} U_p(u), \quad \text{(A.11)}$$

where the α_{pn} and β_{pn} are unknown complex constants (Renzi and Dias, 2012). Substituting (A.11) into the hypersingular integral equation (A.10) yields

$$\sum_{p=0}^{\infty} \left\{ \begin{array}{c} \alpha_{pn} \\ \beta_{pn} \end{array} \right\} C_{pn}(v) = -\pi \left\{ \begin{array}{c} f_n \\ d_n \end{array} \right\} \tag{A.12}$$

where

$$C_{pn} = -\pi(p+1)U_p(v) + \frac{i\pi\kappa_n}{4} \int_{-1}^{1} (1-u^2)^{1/2} U_p(u) \left[\frac{R_n\left(\frac{1}{2}\kappa_n|v-u|\right)}{|v-u|} + L_n(u) \right] du, \tag{A.13}$$

with $v \in (-1, 1)$. In order to solve it numerically, the linear system (A.12) can be truncated to a finite number of terms, evaluated at

$$v = v_{0j} = \cos\frac{(2j+1)\pi}{2P+2}, \quad j = 0, 1, ..., P, \tag{A.14}$$

for fast numerical convergence. This produces two $(P+1)\times(P+1)$ truncated algebraic systems for each n, which are finally solved to determine α_{pn} and β_{pn}. This, together with (A.11), (A.5), (A.4) and (16) allows to calculate the complex spatial potentials (25) and (26).

References

Aquamarine Power Limited, 2012. Lewis wave power 40 MW Oyster wave array non technical summary. www.aquamarinepower.com .

Dean, R.G., Dalrymple, R.A., 1991. Water wave mechanics for engineers and scientists. World Scientific Publishing Company Incorporated.

Evans, D., 1988. The maximum efficiency of wave-energy devices near coast lines. Appl. Ocean Res. 10, 162–164.

Evans, D., Porter, R., 1996. Hydrodynamic characteristics of a thin rolling plate in finite depth of water. Appl. Ocean Res. 18, 215–228.

Falnes, J., 2002. Ocean Waves and Oscillating Systems. Cambridge University Press.

Gradshteyn, I., Ryzhik, I., 2007. Table of integrals, series and products .

Linton, C.M., Evans, D.V., 1993. Hydrodynamic characteristics of bodies in channels. J. Fluid Mech. 252, 647–647.

Linton, C.M., McIver, P., 2001. Handbook of mathematical techniques for wave/structure interactions. Chapman & Hall/CRC.

Lovas, S., Mei, C.C., Liu, Y., 2010. Oscillating water column at a coastal corner for wave power extraction. Appl. Ocean Res. 32, 267–283.

Martins-Rivas, H., Mei, C., 2009. Wave power extraction from an oscillating water column along a straight coast. Ocean Eng. 36, 426–433.

Mei, C., 1997. Mathematical Analysis in Engineering. Cambridge University Press.

Mei, C., Stiassnie, M., Yue, D., 2005. Theory and Applications of Ocean Surface Waves. World Scientific.

Renzi, E., Abdolali, A., Bellotti, G., Dias, F., 2014. Wave-power absorption from a finite array of oscillating wave surge converters. Renewable Energy 63, 55–68.

Renzi, E., Dias, F., 2012. Resonant behaviour of an oscillating wave energy converter in a channel. J. Fluid Mech 701, 482–510.

Renzi, E., Dias, F., 2013a. Hydrodynamics of the Oscillating Wave Surge Converter in the open ocean. Eur. J. Mech. B-Fluid doi:10.1016/j.euromechflu.2013.01.007.

Renzi, E., Dias, F., 2013b. Relations for a periodic array of oscillating wave energy converters. Appl. Ocean Res. 39, 31–39.

Sammarco, P., Michele, S., dErrico, M., 2013. Flap gate farm: From venice lagoon defense to resonating wave energy production. part 1: Natural modes. Applied Ocean Research 43, 206–213.

Sarkar, D., Renzi, E., Dias, F., 2014a. Interactions between an oscillating wave surge converter and a heaving wave energy converter. Journal of Ocean and Wind Energy 1, 135–142.

Sarkar, D., Renzi, E., Dias, F., 2014b. Wave farm modelling of oscillating wave surge converters. Proc. R. Soc. A 470, 20140118.

Srokosz, M., Evans, D., 1979. A theory for wave-power absorption by two independently oscillating bodies. J. Fluid Mech 90, 337–362.

Whittaker, T., Folley, M., 2012. Nearshore oscillating wave surge converters and the development of Oyster. Philos. T. Roy. Soc. A 370, 345–364.